



Originally published as:

Zhou, Y., Lüher, H., Alken, P., Xiong, C. (2016): New perspectives on equatorial electrojet tidal characteristics derived from the Swarm constellation. - *Journal of Geophysical Research*, 121, 7.

DOI: <http://doi.org/10.1002/2016JA022713>

RESEARCH ARTICLE

10.1002/2016JA022713

Key Points:

- This is the first detailed study of the equatorial electrojet (EEJ) based on Swarm satellite data
- The Swarm constellation allows studying the longitudinal gradient of the EEJ
- The longitudinal gradient provides a new perspective on the tidal modulation of the EEJ

Correspondence to:

Y.-L. Zhou,
zhouyl@whu.edu.cn

Citation:

Zhou, Y.-L., H. Lühr, P. Alken, and C. Xiong (2016), New perspectives on equatorial electrojet tidal characteristics derived from the Swarm constellation, *J. Geophys. Res. Space Physics*, 121, 7226–7237, doi:10.1002/2016JA022713.

Received 17 MAR 2016

Accepted 11 JUL 2016

Accepted article online 14 JUL 2016

Published online 28 JUL 2016

New perspectives on equatorial electrojet tidal characteristics derived from the Swarm constellation

Yun-Liang Zhou^{1,2}, Hermann Lühr^{1,2}, Patrick Alken³, and Chao Xiong²

¹Department of Space Physics, School of Electronic Information, Wuhan University, Wuhan, China, ²GFZ German Research Centre for Geosciences, Potsdam, Germany, ³Cooperative Institute for Research in Environmental Sciences, University of Colorado Boulder, Boulder, Colorado, USA

Abstract Using 2 years of magnetic field measurements from the Swarm constellation, we present a detailed study of the equatorial electrojet (EEJ) and its longitudinal gradient (Δ EEJ). This study represents for the first time the tidal characteristics derived from the longitudinal gradient of EEJ. Our analysis mainly focuses on the months around August (133 days centered on 15 August, day of year: 161–293) of 2014 and 2015 when the longitudinal wave number 4 (WN4) pattern is known to be most prominent. The EEJ intensity, derived from the average of the Swarm A and C current estimates, peaks around 11:30 LT and exhibits a clear WN4 pattern. These features are compatible with earlier CHAMP observations. The Δ EEJ, which can be considered as a high-pass filtered result of EEJ, although having much smaller values than the EEJ, exhibits clearly the local time gradient of the EEJ diurnal variation. This kind of high-pass filtering makes the tidal signatures in Δ EEJ more prominent. The crests of longitudinal WN4 patterns in Δ EEJ have locations different from those of EEJ. Prominent tidal components in Δ EEJ during August months are DE3, DW5, SW3, SW4, SW6, SPW1, SPW2, and SPW4. For a given wave number pattern the westward propagating components are more amplified in Δ EEJ than the eastward ones, which explains their numerous appearance. Using spectral analysis, we can confirm that the observed amplitude ratios of different tidal components between Δ EEJ and EEJ are as expected. Also, the phase differences between Δ EEJ and EEJ fit reasonably the theoretical values. The preferred amplification of westward propagating tides in Δ EEJ allows for a more detailed investigation of these components, which are assumed to be closer related to local electrodynamic processes.

1. Introduction

The equatorial electrojet (EEJ) is a narrow belt of prominent electric current flowing typically eastward in the dayside *E* region ionosphere. Due to the relatively low-conducting layers above and below the *E* region and the horizontal magnetic field configuration, a significantly enhanced ionospheric conductivity (termed Cowling conductivity) [Cowling, 1933] can form at the dip equator. The eastward zonal electric field with a typical value of about 0.5 mV/m around noon time [e.g., Fejer *et al.*, 1991] drives the EEJ.

It is well known that the EEJ represents an enhancement of the diurnal variation in the ground geomagnetic recordings near the magnetic dip equator, which was first identified several decades ago at the Huancayo geomagnetic observatory in Peru. Since its discovery many studies of the EEJ have investigated the characteristics and the related physical processes, based on ground magnetometer, rocket magnetometer, and radar observations [e.g., Bartels and Johnston, 1940; Egedal, 1947; Chapman, 1951; Onwumechili, 1967; Fejer *et al.*, 1975; Forbes, 1981]. Global EEJ studies from low-Earth orbit satellites were conducted with observations from the Polar Orbiting Geophysical Observatories satellites [e.g., Onwumechili and Agu, 1980; Agu and Onwumechili, 1981]. Subsequently, an EEJ longitudinal profile, limited to the evening local time sector and the December and March seasons, was obtained from Magsat data [Langel *et al.*, 1993]. Thanks to the launch of satellites like Ørsted, CHAMP, and SAC-C, high-resolution magnetic field data are obtained for all longitudes and local times, which provided a good opportunity to improve our understanding of the EEJ [Jadhav *et al.*, 2002; Ivers *et al.*, 2003; Lühr *et al.*, 2004; Le Mouél *et al.*, 2006; Alken and Maus, 2007]. The recently launched Swarm constellation with its special orbit configuration [Friis-Christensen *et al.*, 2008] allows us to further investigate the characteristics of the EEJ.

Due to the great importance of understanding the ionospheric wind dynamo and electrodynamic processes, the EEJ has drawn significant attention in the past decade. From the magnetic field data of CHAMP the spatial characteristics of the noon-time EEJ were derived [Lühr *et al.*, 2004]. The EEJ is also a suitable proxy for the equatorial electric field, and this contributes to otherwise sparsely available *E* region ionospheric electric field

measurements [Alken and Maus, 2010; Alken et al., 2013, 2015a]. By analyzing the long-term records of ground-based magnetometers in the Indian and Peruvian sectors, the response of EEJ to geomagnetic storms and substorms is found to depend on the magnitude of the storm, solar activity, season, and longitude [Yamazaki and Kosch, 2015]. Based on ground magnetometer data and GPS-TEC data, the importance of EEJ variability for the day-to-day features of the equatorial ionization anomaly (EIA) over the Indian and Brazilian sectors has been studied by Venkatesh et al. [2015]. Their results indicate that the integrated EEJ strength up to the diurnal maximum plays a vital role for the intensity of the EIA. It is furthermore reported that the quiet time day-to-day variability of the EEJ is dominated by the irregular changes of the equatorial neutral wind at 110 km [Yamazaki et al., 2014].

In recent years particular effort has been devoted to study the longitudinal variations of the EEJ. By averaging the EEJ peak current density from August 2000 to April 2003 in longitude bins, it was reported that the current density of the EEJ exhibits a clear longitudinal dependence, showing three distinct intensity peaks at 90°W, 45°W, and 100°E [Lühr et al., 2004]. Also, based on CHAMP satellite observations, England et al. [2006] found that the noontime EEJ around equinoxes exhibits a remarkable wave number 4 (WN4) longitudinal variation, and they suggested that this longitudinal pattern in the EEJ intensity is related to the diurnal eastward propagating tidal component, DE3 (for the tidal nomenclature, see section 4). Besides the WN4 longitudinal structure at equinox seasons the empirical climatological model EEJM-1 based on magnetic observations from the CHAMP, Ørsted, and SAC-C satellites shows, for example, a WN3 structure at December solstice [Alken and Maus, 2007]. By using the aforementioned EEJM-1 model and its second version EEJM-2 (<http://www.geomag.us/models/EEJ.html>) the effects of nonmigrating tides on the EEJ have been investigated [Lühr et al., 2008, 2012]. It is reported that the dominant tidal component for causing EEJ WN4 longitudinal patterns from April to September is DE3, which accounts for about 25% modulation of the total EEJ intensity. The influence of DE3 is negligible during December solstice. Conversely, DE2 is strongest during solstice months. Based on 10 years of magnetic field measurements from CHAMP the complete EEJ spectrum related to solar tides and their annual variation have been presented [Lühr and Manoj, 2013]. They found that the WN4 structure is also caused partly by the diurnal westward propagating tidal component DW5 around August, besides the significant contribution of DE3. During December solstice the semidiurnal westward component SW4 is taking an important role in contributing to the WN2 structures. They also reported that the semidiurnal tide SW3 causes largest EEJ amplitudes from October to December. Recently Xiong et al. [2016] examined the longitudinal wave patterns of the EEJ during quiet and disturbed periods. They found that even during magnetically disturbed periods ($K_p > 3$) the WN4 pattern of the EEJ can still be clearly recognized (especially during September equinox), but with lower amplitudes when compared to quiet periods.

In spite of the many studies on EEJ tidal features, to our knowledge no paper exists which reports the tidal characteristic derived from the EEJ longitudinal gradient. With the recently launched Swarm constellation, especially the pair Swarm A and C, which fly side-by-side, the longitudinal gradient of EEJ between them can be calculated. In this study we make use of the magnetic observations from Swarm A and C to investigate the characteristics of the EEJ and its longitudinal gradient. A detailed quantitative analysis of tidal amplitude and phase changes between EEJ and its longitudinal gradient observations is presented. Addressing these issues provides new insights into the tidal features of the EEJ.

In the next section we will first introduce the Swarm constellation, briefly describe the approach for deriving the EEJ current density from the Swarm magnetic field data, and present the method of tidal analysis for the EEJ and its longitudinal gradient. The obtained results are presented in section 3. Then an interpretation of the tides derived from longitudinal gradients is given in section 4. In section 5 our results are compared and discussed in the context of previous studies. We summarize the main findings in section 6.

2. Data and Processing Approach

2.1. Swarm Constellation

The Swarm constellation, consisting of three spacecraft, primarily aims to measure the Earth's magnetic field and its temporal variation with unprecedented accuracy [Friis-Christensen et al., 2008]. On 22 November 2013 the three spacecraft were launched together into a near-polar orbit (87.5° inclination) with an initial altitude of about 490 km. After a series of orbit maneuvers the final constellation was achieved on 17 April 2014. Since then Swarm A and C fly side-by-side at an altitude of about 470 km and with a longitudinal separation of about 1.4° (about 150 km), which corresponds to about 6 min difference in local time. This longitudinal

separation between Swarm A and C provides a good opportunity to analyze longitudinal gradient characteristics of the EEJ using near-simultaneous measurements. The third satellite Swarm B has a higher altitude of about 520 km at a somewhat higher inclination, causing a slow separation of the orbital planes in local time. Swarm A and C need about 133 days for sampling all local times; for Swarm B it takes about 145 days. The payload complement of each spacecraft includes an absolute scalar magnetometer (ASM), a vector field magnetometer (VFM), an electric field instrument, an accelerometer, and a set of navigation instruments. The data we primarily utilized are the scalar magnetic field measurements made by the ASM onboard Swarm A and C from the period of 17 April 2014 to 16 April 2016. Due to the malfunction of the ASM onboard Swarm C since 5 November 2014, the magnetic field magnitude of Swarm C after this period is derived from the measurements of VFM onboard Swarm C. The Level-1b magnetic field products with time resolution of 1 Hz (product identifier: MAGx_LR) are used, which are available at <http://earth.esa.int/swarm>.

2.2. Derivation of EEJ From Magnetic Data

In this section we will briefly introduce the approach for deriving EEJ current densities from satellite magnetic field data. A detailed description of the approach has been given in previous publications [e.g., Lühr *et al.*, 2004; Alken and Maus, 2007; Alken *et al.*, 2015a].

First, a correction is applied to the magnetic field readings to eliminate the diamagnetic effect caused by pressure gradients in the ambient plasma. The correction formula is given by [Lühr *et al.*, 2003]

$$\Delta B = nk(T_i + T_e) \frac{\mu_0}{B} \quad (1)$$

where n is electron number density measured by the Langmuir Probe onboard Swarm; k is the Boltzmann constant; T_i and T_e are the ion and electron temperatures, respectively; μ_0 is the susceptibility of free space, and B is the magnitude of the ambient magnetic field measured by the magnetometer. In this study the sum of ion and electron temperature is assumed to be a constant value of 2500 K at low latitudes and for all day-time hours. A variation of the temperature has a fairly small influence on the diamagnetic effect. For example, the change of temperature by 500 K causes a change in ΔB of less than 0.5 nT on average.

After the diamagnetic effect correction, the main, crustal, and magnetospheric fields are removed from the magnetic data. A core field model [Alken *et al.*, 2015b] to spherical harmonic degree 15 was constructed from 2 years of Swarm data and is subtracted from the ASM measurements. The crustal field contribution is removed using the MF7 model [Maus *et al.*, 2008], and the external field part of POMME-6 [Lühr and Maus, 2010] is used to remove the magnetospheric fields. Then, the contribution of midlatitude Sq currents, as well as unmodeled external fields, is filtered out on a track-by-track basis using internal and external spherical harmonic field parameterizations, resulting in a clean EEJ signal. Finally, we inverted the obtained EEJ signal for the height-integrated sheet current density by using a model of line currents flowing along lines of constant quasi-dipole latitude at 110 km altitude in the equatorial E region. Since the EEJ signal is too weak during the night, because of the diurnal variation of E region ionospheric conductivity, we limit our analysis to the crossings of the magnetic equator from 06:00 to 18:00 LT.

2.3. Processing Approach

2.3.1. Average Intensity and Longitudinal Gradient of EEJ

As already mentioned, Swarm A and C fly side-by-side and probe the ionosphere simultaneously. The magnetic fields (and resulting EEJ current densities) observed by the two satellites are generally similar. In order to determine the characteristics of the EEJ itself, we consider the average value of the EEJ probed by Swarm A and C. The average EEJ intensity is calculated as

$$EEJ_{ave} = \frac{EEJ_A + EEJ_C}{2} \quad (2)$$

where EEJ_A and EEJ_C are the EEJ peak current densities (on the magnetic equator) in units of mA/m separately derived from Swarm A and C at nearly the same time and position. EEJ_{ave} represents the current density at the midpoint between Swarm A and C, and it is used for analyzing the features of the EEJ.

Although the observations from Swarm A and C are similar, subtle differences still exist between them due to their longitudinal offset. Taking EEJ_A observed at an earlier local time as the reference and subtract it from EEJ_C , we can obtain the difference of the EEJ in the zonal direction, which is labeled ΔEEJ and calculated as

$$\Delta EEJ = EEJ_C - EEJ_A \quad (3)$$

Due to the separation of about 1.4° in longitude between Swarm A and C at the equator, the ΔEEJ reflects features of the EEJ longitudinal gradient. Hereafter we will term this difference (ΔEEJ) as the EEJ longitudinal gradient per 1.4° . For our study we consider the period from April 2014 to April 2016. When taking the whole period, a typical value for the root-mean-square (RMS) value of ΔEEJ is 4.4 mA/m. In order to reject the outliers of the differences we discard the data which exceed the RMS value of the data set by more than 2 times.

2.3.2. Analyzing Tidal Signals

As reported in previous publications the amplitudes of the different tidal components in ionospheric and thermospheric quantities vary with seasons [e.g., Oberheide *et al.*, 2006; Häusler and Lühr, 2009]. In order to analyze the tidal characteristics of the EEJ and ΔEEJ , we sort EEJ_{ave} and ΔEEJ into four seasons. For each season overlapping periods of 133 days, centered on March equinox, June solstice, September equinox, and December solstice days, are considered to make sure that Swarm A and C samples cover all local time hours when considering upleg and downleg passes of the satellites. For this study we take only equator crossings on the dayside into account. For a dedicated determination of the tidal spectral content in ΔEEJ , 133 days centered on 15 August of the 2 years are additionally selected because the WN4 patterns are most prominent during this period of time [e.g., Lühr *et al.*, 2012; Xiong and Lühr, 2013]. In the following, we refer to this period as August months. For each season we bin EEJ_{ave} and ΔEEJ data into local time (1h) by geographic longitude (15°) bins. In order to determine the nonmigrating tidal components the longitudinal mean values have been subtracted hour by hour to suppress the contribution of the migrating tidal components. In this study we restrict our investigation of the EEJ to dayside hours from 06:00 to 18:00 LT. Due to the limited local time range, a rigorous application of a two-dimensional Fourier transform cannot be applied to uniquely decompose all tidal components. We thus use a two-step procedure. First, we fit the longitudinal variations of EEJ and ΔEEJ for every local time hour to a sinusoidal wave function W_m , which is given by

$$W_m = A_m \cdot \cos[m(\lambda - \phi_m)] \quad (4)$$

where A_m is the amplitude of the wave with longitudinal wave number m , λ denotes the longitude, and ϕ_m is the phase value reflecting the longitude of the wave maximum. In this study we consider the wave functions with wave number $m = 1, 2, 3$, and 4. The involved tidal components can be estimated from the distribution of amplitudes and phases in a longitude versus local time frame. In particular, the tilt angle of the phase front and direction (eastward or westward) can be used to identify the dominant tides responsible for the longitudinal pattern. In a second step we fit a set of preselected tidal components, based on a nonlinear least squares method, to the obtained wave functions from equation (4), separately for each wave number. By checking the residual patterns we can iterate our selection.

3. Observations

Figure 1 presents the current densities of the EEJ derived from the average of Swarm A and C current estimates in a longitude versus local time frame separately for the four seasons. In general, the average EEJ shows similar diurnal variations for the different seasons, with peak values around 11:00–12:00 LT. The current flows eastward during most of the daytime (09:00–15:00 LT), with maximum amplitudes of about 150 mA/m, while westward currents are observed in the early morning and late afternoon hours. The westward current indicates the so-called counter equatorial electrojet. Moreover, the EEJ intensity exhibits some prominent longitudinal patterns. In particular, the well-known longitudinal WN4 structure can be seen during June solstice and September equinox seasons. During March equinox it seems that there is a mixture of WN4 and WN3 patterns, while around December solstice the EEJ is dominated by a longitudinal WN3 pattern. In general, the EEJ longitudinal patterns resemble previous results [e.g., Lühr and Manoj, 2013]. Part of the differences may be related to the fact that we only consider 2 years of Swarm measurements.

Figure 2 shows the ΔEEJ derived from Swarm A and C in a longitude versus local time frame for different seasons. Compared with the full EEJ signature from Swarm A and C the amplitudes of ΔEEJ are as expected much lower. The range of ΔEEJ values is about ± 5 mA/m, which is about 25 times smaller than that of the EEJ. In general, ΔEEJ is mainly positive from 06:00 to 11:00 LT and negative values dominate from 12:00 to 18:00 LT, with peak values around 10:00 LT. A positive (negative) value of ΔEEJ denotes an EEJ increases (decrease) with local time. The ΔEEJ peaks around 10:00 LT are denoting the largest increasing gradient of the EEJ at this

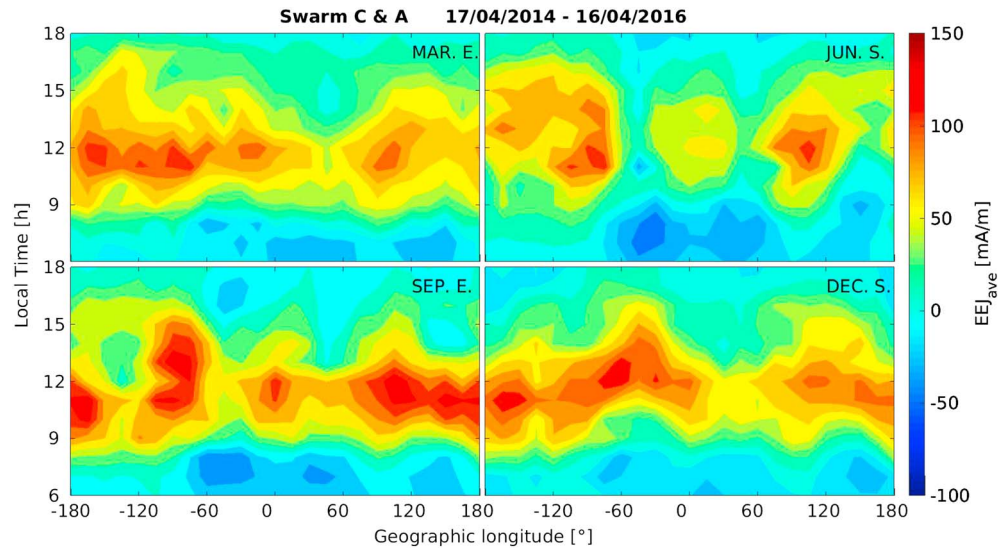


Figure 1. The local time versus longitude variations of the average EEJ observed by Swarm A and C during four seasons.

local time. The negative values of ΔEEJ after 12:00 LT imply that the EEJ in the *E* region stops to increase around noon. It is interesting to note that the EEJ at certain times and locations keeps intensifying till 15:00 LT (at 120°W longitude around September equinox). Moreover, the local time versus longitude distribution of ΔEEJ shows clear longitudinal patterns during all seasons. In contrast to the full EEJ, the ΔEEJ exhibits some WN4 patterns at all four seasons, especially during June solstice and September equinox.

Earlier studies have revealed the largest tidal amplitudes around the months of August [e.g., *Lühr and Manoj, 2013*]. In order to demonstrate the tidal effects on the EEJ longitudinal gradient we focus here on this period of the year. As mentioned before, we select the 133 days centered on 15 August (day of year: 161–293) to investigate all prominent tidal components. The longitude versus local time distributions of EEJ and ΔEEJ during the August months are presented in Figure 3. The four wave maxima are well separated during this period. Compared with Figures 1 and 2, a clearer WN4 pattern can be identified during August months both in the electrojet intensity and in the gradient. The crests of WN4 pattern for EEJ during this period are located

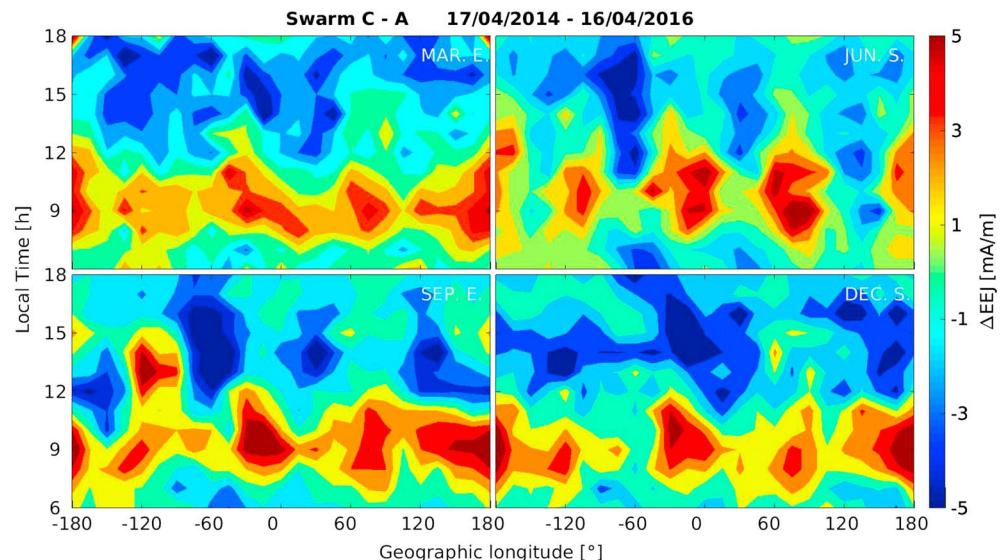


Figure 2. The same as Figure 1 but for the ΔEEJ .

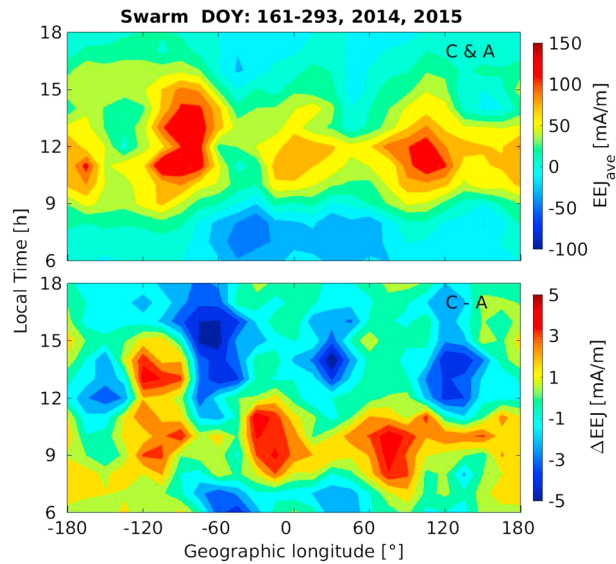


Figure 3. The local time versus longitude variations of the EEJ and Δ EEJ observed by Swarm A and C around August months of 2014 and 2015.

at about -180° , -90° , 0° , and 90° in longitude. While for the WN4 crests in Δ EEJ they appear at about -120° , -15° , 75° , and 165° .

For the determination of the nonmigrating tidal signals of Δ EEJ we first subtract the longitudinal mean value hour by hour, in order to suppress the migrating tides. The longitudinal mean-free Δ EEJ variations are shown in a local time versus longitude frame in Figure 4a. In a next step we try to remove the effect of the diurnal variation of the E layer conductivity represented by the function $[\cos(\frac{\pi}{12}(LT - 12.5))]^{1/2}$ as suggested by Lühr *et al.* [2008]. The Δ EEJ values normalized to the peak conductivity at 12:30 LT are presented in Figure 4 b. It should be noted that we truncated the LT range from 08:00 to 17:00 LT, in order to avoid too strong modification of the observations by the scaling function. A WN4 pattern can clearly be seen in Figures 4a and 4b. In addition, a westward propagating longitudinal pattern is also evident. This implies that a significant amount of interference takes place between different tidal components. In order to obtain detailed information of the various tidal signals in the mean-free Δ EEJ we apply the method described in section 2. First, we filter by applying equation (4) to each local time hour bin and obtain the first four wave number patterns, namely, WN1 to WN4. The obtained pattern for WN4 is presented in Figure 4c. Figure 5 shows the longitude versus local time distributions of the WN1 and WN2 patterns. It should be mentioned that the wave amplitude for WN3 is not shown here, as no coherent signal is obtained. The results provide a good overview of the tidal wave content present in Δ EEJ. From Figure 4c

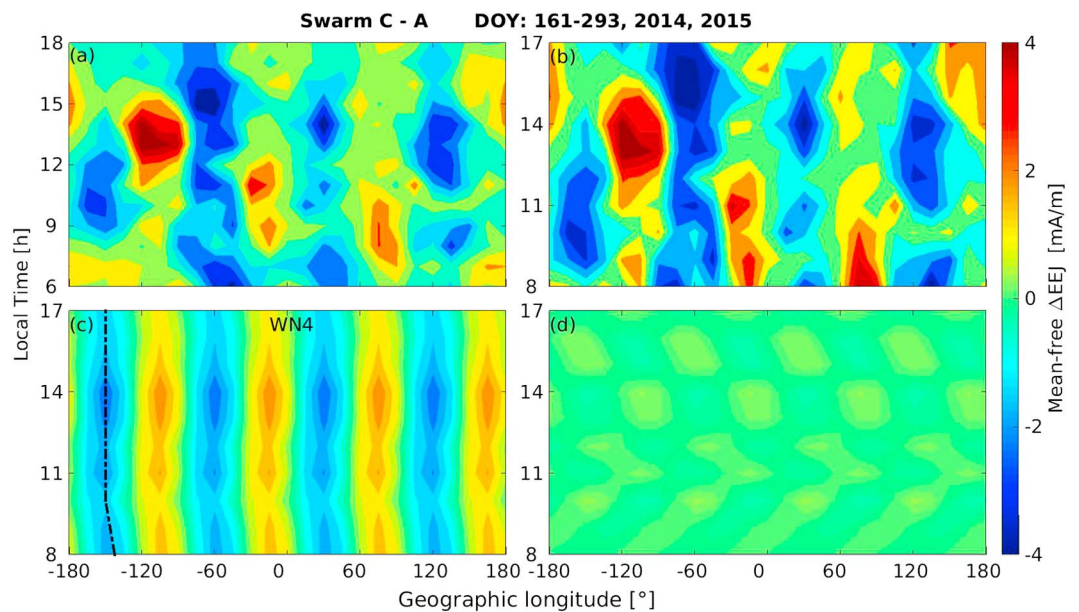


Figure 4. The local time versus longitude variations of (a) mean-free Δ EEJ, (b) mean-free Δ EEJ after removing the effect of the changing E layer conductivity, (c) the WN4 pattern, and (d) the residuals of WN4 pattern after fitting the tidal components DE3, DW5, SW6, and SPW4 during August months of 2014 and 2015. The black dashed lines in Figure 4c indicate the phase propagation of DW5 and SPW4.

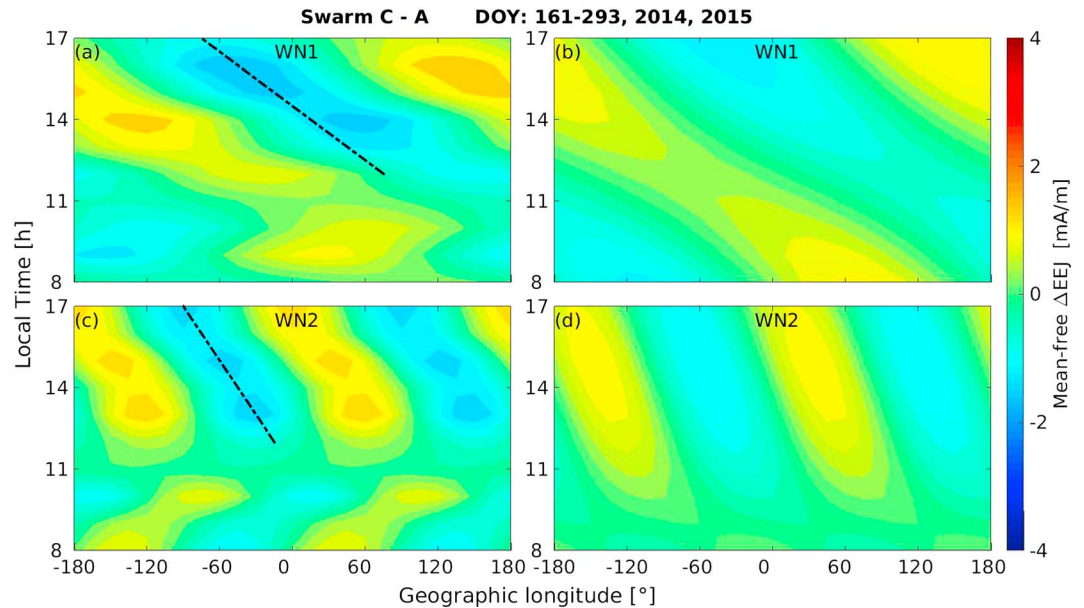


Figure 5. The local time versus longitude variations of (a) WN1 pattern, (b) signals of SW3 and SPW1, (c) WN2 pattern, and (d) signals of SW4 and SPW2 during August months of 2014 and 2015. The black dashed lines in Figures 5a and 5c indicate the phase propagation of SW3 and SW4, respectively.

we see that WN4 exhibits amplitudes of about 2 mA/m. It is interesting to note that during the morning hours, up to 10:00 LT, the WN4 phase shifts westward by about 7.5° in longitude within 2 h of local time, which matches the tilt angle of DW5. From 11:00 to 17:00 LT the wave crests stay at the same longitude resembling SPW4 during that part of the day. The expected phase shifts for DW5 and SPW4 are indicated by dashed black lines in Figure 4c. Depicted in Figure 5a is the WN1 pattern of the mean-free ΔEEJ, which is dominated by westward tilted features. The peak value of the WN1 pattern amplitude is about 1 mA/m. It is evident that the WN1 pattern propagates westward about 180° in longitude within 6 h of local time. This tilt angle agrees with the phase shift of the SW3 tidal component, as indicated by the black dashed line in Figure 5a. This suggests SW3 to be the main contributor to the observed westward WN1 pattern in ΔEEJ. When looking at the WN2 pattern, as shown in Figure 5c, the maximum value of the WN2 pattern amplitude amounts also to about 1 mA/m between 13:00 and 17:00 LT. It can be seen that the WN2 pattern propagates westward by about 90° in longitude within 6 h in local time, which is in line with the phase propagation of SW4, as indicated by the black dashed line in Figure 5c. This tilt angle of phase front demonstrates the dominance of the SW4 tidal component in WN2 structure during the afternoon hours. In contrast, no clear tidal phase pattern is observed during the hours around 12:00 LT.

4. Interpretation of the Tidal Signatures in ΔEEJ

As mentioned above, the longitudinal patterns of EEJ and ΔEEJ can be caused by different tidal components. From the perspective of an observer on the Earth surface the tidal modulation of the EEJ in universal time (UT) frame can be expressed by an expansion of harmonic terms [e.g., Forbes et al., 2006; Häusler and Lühr, 2009]

$$EEJ = \sum_{n,s} A_{n,s} \cos(n\Omega t + s\lambda - \phi_{n,s}) \quad (5)$$

where t is the universal time; Ω is the rotation rate of the Earth ($\Omega = \frac{2\pi}{24 \text{ h}}$); λ is the longitude, n ($n = 1, 2, 3, \dots$) is the harmonic of a solar day, diurnal tides are $n = 1$, semidiurnal tides are $n = 2$; and s is the zonal wave number in UT frame. For westward propagating tides s is positive and negative for eastward. $A_{n,s}$ is the amplitude, and $\phi_{n,s}$ is the phase in units of radians, which can be regarded as the UT time at which the wave maximum passes the zero-degree longitude. In order to label various tidal components, we use the convention where the first letter D (S) denotes the diurnal (semidiurnal) tides, the second letter E (W) stands for eastward (westward) tides, and the last number is for the zonal wave number. The stationary planetary wave (for $n=0$) is labeled SPWs, where s is the zonal wave number.

The signal of ΔEEJ represents the derivative of the EEJ longitudinal variation. According to equation (5) the ΔEEJ can therefore be described as

$$\Delta EEJ = -\sum_{n,s} A_{n,s} \cdot s \cdot \Delta\lambda \cdot \sin(n\Omega t + s\lambda - \phi_{n,s}) \quad (6)$$

where $\Delta\lambda$ is the 1.4° , the longitudinal separation between Swarm A and C. Near-polar-orbiting satellites sample the EEJ at almost fixed local time. When expressing the tidal signatures in a local time frame equation (5) becomes

$$EEJ = \sum_{n,s} A_{n,s} \cdot \cos(n\Omega t_{LT} + (s-n)\lambda - \phi_{n,s}) \quad (7)$$

where t_{LT} ($t_{LT} = t + \lambda/\Omega$) is the local time, $|s-n|$ is the longitudinal wave number of tides in the longitude versus local time frame, and $\phi_{n,s}$ is the tidal phase. Similarly, in the local time frame equation (6) becomes

$$\Delta EEJ = -\sum_{n,s} A_{n,s} \cdot s \cdot \Delta\lambda \cdot \sin(n\Omega t_{LT} + (s-n)\lambda - \phi_{n,s}) \quad (8)$$

For eastward tides ($s < 0$), equation (8) can be written as

$$\Delta EEJ = \sum_{n,s} A_{n,s} \cdot |s| \cdot \Delta\lambda \cdot \cos\left(n\Omega t_{LT} + (s-n)\lambda - \phi_{n,s} - \frac{\pi}{2}\right) \quad (9)$$

While for westward tides ($s > 0$), equation (8) can be written as

$$\Delta EEJ = \sum_{n,s} A_{n,s} \cdot s \cdot \Delta\lambda \cdot \cos\left(n\Omega t_{LT} + (s-n)\lambda - \phi_{n,s} + \frac{\pi}{2}\right) \quad (10)$$

Comparing equation (7) with equations (9) and (10), the differences in amplitude and phase for the various tidal components between EEJ and ΔEEJ can be estimated. First, we can see that the amplitude ratio of ΔEEJ to EEJ is $|s| \cdot \Delta\lambda$, which is proportional to the wave numbers and also related to the separation in longitude (here $\Delta\lambda$ is 1.4° in longitude). When decomposing a given wave number pattern in local time frame the westward components have larger s values than the eastward. For example, the diurnal tides DW5 and DE3 contribute both to the WN4 longitudinal pattern. Thus, the westward components are more amplified than eastward ones in ΔEEJ . On the other hand, the phases of tidal components are different in ΔEEJ from EEJ. For westward components in ΔEEJ the phases are earlier than those of EEJ with the value of $\frac{\pi}{2n\Omega} = \frac{6}{n}$ in local time hours. However, for eastward components the phases are later by the same value of $\frac{6}{n}$. Therefore, for westward diurnal components the phases appear 6 h earlier in ΔEEJ , 3 h earlier for westward semidiurnal tides, 6 h later for eastward diurnal components, and so on. For planetary waves ($n=0$) the phase shifts of ΔEEJ will lead to $\frac{\pi}{2s}$ (radians) in longitude. Taking the component SPW4 as an example the phase of ΔEEJ will lead that of the EEJ by 22.5° in longitude. The tidal phase changes result in the different locations of wave maxima between EEJ and ΔEEJ .

For a quantitative analysis of amplitudes and phases of the various tidal components in the EEJ and ΔEEJ , we fitted the dominant tidal components estimated from the tilt angles of phase fronts in Figures 4 and 5 of the WN1, WN2, and WN4 patterns. The choice of selected tidal components is confirmed by checking the residuals. Taking WN4 as an example, the residuals of the WN4 pattern after fitting the tidal components of DE3, DW5, SW6, and SPW4 are small and scatter randomly. The amplitudes and phases of all considered tides derived for EEJ and ΔEEJ are listed in Table 1. Additionally, the observed and theoretically expected amplitude ratios and phase delays between EEJ and ΔEEJ for the considered tidal components are presented in Table 1. It has to be noted that a negative phase delay represents phase lead. From the numbers listed in Table 1 it can be seen that generally, the observations agree well with the expected results. For signals of SW3 and SPW1 components, which contribute to the WN1 pattern, the amplitude ratios are in good agreement with the theoretical values. For completeness the signals of SW3 and SPW1 are presented in Figure 5 b. For the WN2 pattern the amplitude ratio and the phase lead of SPW2 from observations are well in line with their expectation values. In spite of the larger phase lead of SW4 than expected, its amplitude ratio matches well the theoretical value. The phase lead of SW4 is off by about 0.9 h, which may be caused by the complicated structure of WN2 during 08:00–09:00 LT, as depicted in Figure 5c. The signals of SW4 and SPW2 are shown in Figure 5d. The tidal components DE3, DW5, SW6, and SPW4 contribute to the WN4 structure of

Table 1. The Decomposed Amplitudes and Phases of Prominent Tidal Components From the EEJ and ΔEEJ^a

Tides	EEJ		ΔEEJ		Observation		Expectation	
	Amp. (mA/m)	Phase	Amp. (mA/m)	Phase	Amp. Ratio	Phase Delay	Amp. Ratio	Phase Delay
DE3	16.39	11.80 h	1.07	19.14 h	0.066	7.34 h	0.073	6 h
DW5	21.94	11.11 h	2.00	5.52 h	0.091	-5.59 h	0.122	-6 h
SW6	7.57	5.51 h	0.80	2.90 h	0.106	-2.61 h	0.146	-3 h
SPW4	14.01	29.88°	1.38	6.27°	0.098	-23.61°	0.098	-22.5°
SW4	6.43	9.03 h	0.61	5.13 h	0.094	-3.90 h	0.098	-3 h
SPW2	12.43	78.96°	0.51	34.01°	0.041	-44.95°	0.049	-45°
SW3	11.27	13.31 h	0.87	9.69 h	0.077	-3.62 h	0.073	-3 h
SPW1	16.87	210.26°	0.33	116.58°	0.020	-93.68°	0.025	-90°

^aIn addition, amplitude ratios and phase delays of tides are compared between the observation and expectation.

ΔEEJ . For SPW4 the phase lead and amplitude ratio fits well the expectation. In general, all the observed amplitudes and phase differences for the other tides contributing to WN4 are in reasonable agreement with their theoretical values (see Table 1).

5. Discussion

5.1. The Features of the EEJ and Its Local Time Gradient Observed by Swarm

In this paper we present the first comprehensive report on EEJ and its longitudinal gradient variations observed by Swarm A and C. For completeness Figure 6 (top) shows for August months the local time variations of the EEJ averaged over all longitudes. It can be seen that the longitudinally averaged EEJ peaks at about 80 mA/m around 11:00 LT. These values are fully compatible with those obtained about 10 years earlier by CHAMP [e.g., Lühr et al., 2008] and with those derived from the EEJM-1 model [Alken and Maus, 2007], when considering the season and the average solar flux level ($F_{10.7} = 123$ solar flux unit). From Figure 6 we see that the EEJ intensity rises steeply between 08:00 and 11:00 LT and decreases gradually thereafter. During the morning hours both the eastward electric field and the conductivity rise. Around 11:00 LT the E field has reached its peak value while the conductivity continues to rise until afternoon. This difference in phasing is the reason for the slower EEJ decay in the afternoon.

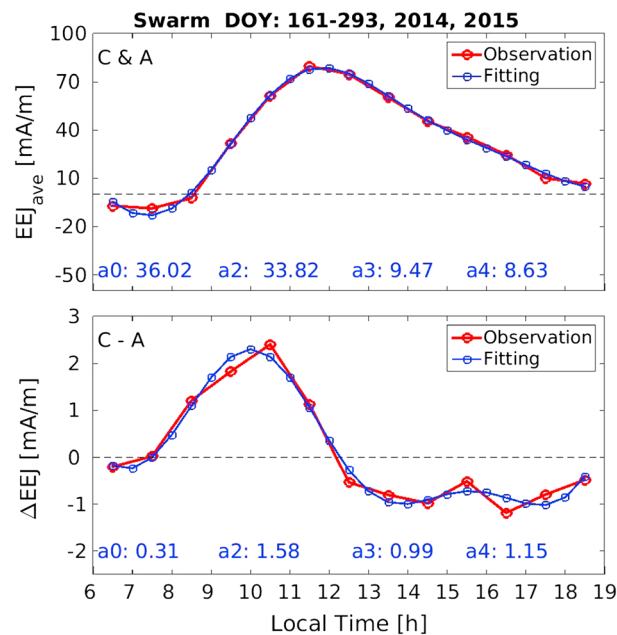


Figure 6. The local time variations of longitudinal average of EEJ and ΔEEJ for August months (red curves). The fitting local time variations based on the first four harmonics are depicted as blue curves. The blue text indicates the fitted amplitudes (in units of mA/m) of the first four harmonics.

Figure 6 (bottom) shows the average of the EEJ longitudinal gradient, representing the local time change rate. A smooth curve (in blue), based on the first four harmonics of a day, has been fitted to the observations. The amplitudes of the harmonics, including the constant, semidiurnal, terdiurnal, and quarter diurnal terms, are also listed in Figure 6. It should be mentioned that the diurnal term cannot be computed because we have data only for 12 local time hours. The differences between Swarm C and A confirm well the rapid rise of the EEJ during prenoon hours with steepest gradient around 10:00 LT. The zero crossing at 12:00 LT marks the start of EEJ decline. The minor peak around 15:30 LT can be related

to the effect of the SW3 tide (see next section). In spite of the small amplitudes all the features derived from the differences seem to be reliable.

One issue to be discussed is the reliability of the presented results, in particular those derived from the difference between Swarm A and C. It is known that the EEJ exhibits a considerable amount of day-to-day variability. For that reason the standard deviation of the bin averages shown in Figure 3 reaches about 50% of the mean value for the EEJ and about 80% for the Δ EEJ. More important for this study is the uncertainty of the mean value, which is derived by dividing the standard deviation by the square root of independent EEJ readings contributing to a bin average. By this procedure we obtain uncertainties of about 6% for EEJ results, and for the Δ EEJ data the uncertainty is generally smaller than 0.6 mA/m. These values show that it is not justified to extend the tidal analysis to components beyond the ones presented in Table 1, which are expected to have smaller amplitudes.

For the longitudinal and local time distribution of the EEJ from Swarm A/C around August months (see Figure 3, top), the observations show a clear WN4 pattern having wave maxima centered at about -180° , -90° , 0° , and 90° in longitude. The maxima over South America and Indonesia are stronger. These features are in good agreement with the results from CHAMP [see Lühr *et al.*, 2012, Figure 2]. The similar results from the two independent missions support the inference that these are persistent features of the EEJ. The WN4 patterns of EEJ have been reported before [e.g., England *et al.*, 2006; Lühr *et al.*, 2012], which can be attributed to the upward propagation of tidal components, such as DE3 from the lower atmosphere to the upper atmosphere, either by direct propagation or through the *E* region wind coupling mechanism [e.g., Wu *et al.*, 2012]. It is reported that the latent heat released from deep convection in the tropical troposphere is the main source of DE3 tides [Hagan and Forbes, 2002], which results in the WN4 patterns of ionospheric quantities at low and equatorial latitudes.

5.2. Tidal Characteristic of Δ EEJ

In this study we go one step further than just interpreting the tidal features of EEJ modulation. By considering for the first time the longitudinal gradient of the electrojet intensity, additional information can be derived. An obvious effect of the difference is the amplification of tides with larger wave numbers. Some important tidal components become visible in the Δ EEJ data without special treatment (see Figures 4 and 5). From these figures it becomes clear why there is prominent EEJ activity even in the afternoon over the Pacific Ocean (west of 90° W). It is just the constructive interference between the DE3 and SW3 tides.

Many studies have stressed the dominance of the DE3 tide in modulating the EEJ. Besides the dominant DE3 component, Lühr and Manoj [2013] reported that the DW5 component is also strong surmounting other diurnal nonmigrating tidal components during August months (see their Figure 5). Here we obtain a somewhat different picture. As outlined in section 4 the westward propagating tides are preferably enhanced in Δ EEJ data. Therefore, the role of DW5 becomes rather clear here. From the angle of phase propagation in Figure 4c we see that DW5 signatures dominate WN4 pattern during morning hours up to 10:00 LT. During later hours the WN4 wavefronts fit more to SPW4. The presence of SPW4 has been explained by Hagan *et al.* [2009] as an interference product between the diurnal migrating tide DW1 and the nonmigrating DE3. The change in wavefront tilt obvious in Figure 4c is a consequence of constructive and destructive interferences of different tidal components. A good representation of the observed WN4 in Δ EEJ could only be achieved by including the tidal components DE3, DW5, SW6, and SPW4. From Table 1 we can see that DE3 and SPW4 have comparable amplitudes in the EEJ, while in Δ EEJ the SPW4 is more strongly amplified. The SW6 is not so important in EEJ but largely amplified in Δ EEJ.

A change in wavefront orientation is also observed in the WN2 pattern before noon (see Figure 5c). A clear longitudinal pattern fitting SW4 emerges in the afternoon hours. In order to get a reasonable fit for all hours we had to introduce the planetary wave SPW2. As can be seen from Table 1, both tidal components are of comparable importance in Δ EEJ.

The prominent WN1 pattern in Figure 5a can be related over the whole day to the SW3 tide. The SW3 seems to be a tidal component rather common in the ionosphere. Lühr *et al.* [2012] had identified it as the dominating tide in vertical plasma drift during August months at day time (see their Table 1). This clearly suggests a generation mechanism at *E* layer level. Xiong and Lühr [2013] reported about the SW3 signature in the low-latitude *F* region electron density and found a strong dependence on solar EUV flux level. This indicates that SW3 prefers the denser ionosphere and thermosphere, i.e., times of closer coupling between ion and neutral

dynamics. Also, Lühr and Manoj [2013] confirmed the dependence of SW3 on solar activity in their EEJ study. This tide seems to be closely related to the electrodynamics of the ionosphere. The Δ EEJ signal may be particularly suitable for studying it in more detail.

It is interesting to note that no coherent tidal signal could be observed in the Δ EEJ WN3 pattern. This means that the eastward propagating tide DE2 must have been quite weak during the considered months. DE2 is also thought to be excited by deep tropospheric convection, but peaking mainly during solstice months. The low wave number furthermore does not help to make it more visible in Δ EEJ.

By jointly interpreting EEJ and its longitudinal gradient the tidal characteristics in the EEJ become much clearer. As more data become available from the Swarm mission this approach should be applied to all seasons with special emphasis on westward propagating tides.

6. Summary

We have presented for the first time a detailed investigation of the EEJ derived from the Swarm constellation. The EEJ signals presented here are derived from the magnetic field measured by Swarm A and C. Of particular interest in the presented study are the tidal characteristics of the EEJ longitudinal gradient (Δ EEJ), which have not been addressed before. Our major findings are outlined as follows:

1. The EEJ signals derived from Swarm A and C are fully compatible with those obtained by CHAMP. We find that the EEJ peaks around 11:00 LT with maximum amplitudes of about 150 mA/m, and it decreases gradually thereafter. A clear longitudinal WN4 pattern is exhibited during August months, showing crests centered at about -180° , -90° , 0° , and 90° in longitude.
2. Compared with the full EEJ signature, the Δ EEJ over a distance of 1.4° in longitude is much smaller exhibiting values in the range of ± 5 mA/m. The Δ EEJ value rises steeply between 07:00 and 09:00 LT reaching its maximum value around 10:00 LT. Around 12:00 LT it switches sign from positive to negative. In spite of its small amplitudes, the Δ EEJ confirms well the diurnal variations of EEJ.
3. In a local time versus longitude frame the Δ EEJ during August months shows a clear WN4 pattern with the crests centered at about -120° , -15° , 75° , and 165° . In contrast to the EEJ, obvious westward propagating features are revealed in the Δ EEJ. It is found that SW3, SW4, SW6, DW5, DE3, SPW1, SPW2, and SPW4 tidal components take important roles in constituting the Δ EEJ longitudinal pattern.
4. A detailed quantitative analysis of tidal amplitude and phase changes between EEJ and Δ EEJ observations is presented. The amplitude ratio of various tidal components between Δ EEJ and EEJ is proportional to the zonal wave number, which demonstrates that for a given wave number pattern the westward propagating components are more amplified than eastward ones in Δ EEJ.
5. The phase changes between Δ EEJ and EEJ have an inverse proportionality to the harmonic of a solar day. For the westward tidal components the phases are earlier in Δ EEJ than in EEJ, while later for the eastward ones. The different locations of longitudinal wave maxima between EEJ and Δ EEJ are related to the tidal phase changes.

In conclusion we can state that the interpretation of the EEJ longitudinal gradient provides new opportunities for investigating the westward propagating tides. These may provide new clues about the electrodynamics of the ionosphere.

Acknowledgments

The authors thank the European Space Agency for providing the Swarm data, which are available at <http://earth.esa.int/swarm>. New users have to register in order to get an account. The work of Yun-Liang Zhou is supported by the National Nature Science Foundation of China (41274194 and 41431073) and China Scholarship Council (201506275011).

References

- Agü, C. E., and C. A. Onwumechili (1981), Comparison of the POGO and ground measurements of the magnetic field of the equatorial electrojet, *J. Atmos. Terr. Phys.*, *43*, 801–907, doi:10.1016/0021-9169(81)90057-X.
- Alken, P., and S. Maus (2007), Spatio-temporal characterization of the equatorial electrojet from CHAMP, Ørsted, and SAC-C satellite measurements, *J. Geophys. Res.*, *112*, A09305, doi:10.1029/2007JA012524.
- Alken, P., and S. Maus (2010), Electric fields in the equatorial ionosphere derived from CHAMP satellite magnetic field measurements, *J. Atmos. Sol. Terr. Phys.*, *72*, 319–326, doi:10.1016/j.jastp.2009.02.006.
- Alken, P., S. Maus, P. Vigneron, O. Sirol, and G. Hulot (2013), Swarm SCARF equatorial electric field inversion chain, *Earth Planets Space*, *65*(11), 1309–1317, doi:10.5047/eps.2013.09.008.
- Alken, P., S. Maus, A. Chulliat, P. Vigneron, O. Sirol, and G. Hulot (2015a), Swarm equatorial electric field chain: First results, *Geophys. Res. Lett.*, *42*, 673–680, doi:10.1002/2014GL062658.
- Alken, P., S. Maus, A. Chulliat, and C. Manoj (2015b), NOAA/NGDC candidate models for the 12th generation International Geomagnetic Reference Field, *Earth Planets Space*, *67*, 68, doi:10.1186/s40623-015-0215-1.
- Bartels, J., and H. F. Johnston (1940), Geomagnetic tides in horizontal intensity at Huancayo, Part I, terrestrial magnetism and atmospheric electricity, *J. Geophys. Res.*, *45*, 269–308, doi:10.1029/TE045i003p0269.

- Chapman, S. (1951), The equatorial electrojets detected from the abnormal electric currents distribution over Huancayo, Peru and elsewhere, *Arch. Meteorol. Geophys. Bioclimatol. Ser. A*, *4*, 368–390.
- Cowling, T. G. (1933), The electrical conductivity of an ionized gas in the presence of a magnetic field, *Mon. Not. R. Astron. Soc.*, *93*, 90–98, doi:10.1093/mnras/93.1.90.
- Egedal, J. (1947), The magnetic diurnal variation of the horizontal force near the magnetic equator, *Terr. Magn. Atmos. Electr.*, *52*, 449–451, doi:10.1029/TE052i004p00449.
- England, S. L., S. Maus, T. J. Immel, and S. B. Mende (2006), Longitudinal variation of the E-region electric fields caused by atmospheric tides, *Geophys. Res. Lett.*, *33*, L21105, doi:10.1029/2006GL027465.
- Fejer, B. G., D. T. Farley, B. B. Balsley, and R. F. Woodman (1975), Vertical structure of the VHF backscattering region in the equatorial electrojet and the gradient drift instability, *J. Geophys. Res.*, *80*(10), 1313–24, doi:10.1029/JA080i010p01313.
- Fejer, B. G., E. R. De Paula, S. A. Gonzales, and R. F. Woodman (1991), Average vertical and zonal F region plasma drifts over Jicamarca, *J. Geophys. Res.*, *96*, 13,901–13,906, doi:10.1029/91JA01171.
- Forbes, J. M. (1981), The equatorial electrojet, *Rev. Geophys.*, *19*, 469–504, doi:10.1029/RG019i003p00469.
- Forbes, J. M., J. Russell, S. Miyahara, X. Zhang, S. Palo, M. Mlynczak, C. J. Mertens, and M. E. Hagan (2006), Troposphere-thermosphere tidal coupling as measured by the SABER instrument on TIMED during July–September 2002, *J. Geophys. Res.*, *111*, A10S06, doi:10.1029/2005JA011492.
- Friis-Christensen, E., H. Lühr, D. Knudsen, and R. Haagmans (2008), Swarm–An Earth observation mission investigating geospace, *Adv. Space Res.*, *41*(1), 210–216, doi:10.1016/j.asr.2006.10.008.
- Hagan, M. E., and J. M. Forbes (2002), Migrating and nonmigrating diurnal tides in the middle and upper atmosphere excited by tropospheric latent heat release, *J. Geophys. Res.*, *107*(D24), 4754, doi:10.1029/2001JD001236.
- Hagan, M. E., A. Maute, and R. G. Roble (2009), Tropospheric tidal effects on the middle and upper atmosphere, *J. Geophys. Res.*, *114*, A01302, doi:10.1029/2008JA013637.
- Häusler, K., and H. Lühr (2009), Nonmigrating tidal signals in the upper thermospheric zonal wind at equatorial latitudes as observed by CHAMP, *Ann. Geophys.*, *27*, 2643–2652, doi:10.5194/angeo-27-2643-2009.
- Ivers, D., Stening, R., Turner, J., and Winch, D. (2003), Equatorial electrojet from Ørsted scalar magnetic field observations, *J. Geophys. Res.*, *108*(A2), 1061, doi:10.1029/2002JA009310.
- Jadhav, G., Rajaram, M., and Rajaram, R. (2002), A detailed study of equatorial electrojet phenomenon using Ørsted satellite observations, *J. Geophys. Res.*, *107*(A8), 1175, doi:10.1029/2001JA000183.
- Langel, R. A., M. Purucker, and M. Rajaram (1993), The equatorial electrojet and associated currents as seen in Magsat data, *J. Atmos. Terr. Phys.*, *55*, 1233–1269, doi:10.1016/0021-9169(93)90050-9.
- Le Mouél, J.-P., P. Shebalin, and A. Chulliat (2006), The field of the equatorial electrojet from CHAMP data, *Ann. Geophys.*, *24*, 515–527, doi:10.5194/angeo-24-515-2006.
- Lühr, H., and C. Manoj (2013), The complete spectrum of the equatorial electrojet related to solar tides: CHAMP observations, *Ann. Geophys.*, *31*, 1315–1331, doi:10.5194/angeo-31-1315-2013.
- Lühr, H., and S. Maus (2010), Solar cycle dependence of quiet-time magnetospheric currents and a model of their near-Earth magnetic fields, *Earth Planets Space*, *62*, 843–848, doi:10.5047/eps.2010.07.012.
- Lühr, H., M. Rother, S. Maus, W. Mai, and D. Cooke (2003), The diamagnetic effect of the equatorial Appleton anomaly: Its characteristics and impact on geomagnetic field modeling, *Geophys. Res. Lett.*, *30*(17), 1906, doi:10.1029/2003GL017407.
- Lühr, H., S. Maus, and M. Rother (2004), Noon-time equatorial electrojet: Its spatial features as determined by the CHAMP satellite, *J. Geophys. Res.*, *109*, A01306, doi:10.1029/2002JA009656.
- Lühr, H., M. Rother, K. Häusler, P. Alken, and S. Maus (2008), The influence of nonmigrating tides on the longitudinal variation of the equatorial electrojet, *J. Geophys. Res.*, *113*, A08313, doi:10.1029/2008JA013064.
- Lühr, H., M. Rother, K. Häusler, B. Fejer, and P. Alken (2012), Direct comparison of non-migrating tidal signatures in the electrojet, vertical plasma drift and equatorial ionization anomaly, *J. Atmos. Sol. Terr. Phys.*, *75–76*, 31–43, doi:10.1016/j.jastp.2011.07.009.
- Maus, S., F. Yin, H. Lühr, C. Manoj, M. Rother, J. Rauberg, I. Michaelis, C. Stolle, and R. D. Müller (2008), Resolution of direction of oceanic magnetic lineations by the sixth-generation lithospheric magnetic field model from CHAMP satellite magnetic measurements, *Geochem. Geophys. Geosyst.*, *9*, Q07021, doi:10.1029/2008GC001949.
- Oberheide, J., Q. Wu, T. L. Killeen, M. E. Hagan, and R. G. Roble (2006), Diurnal nonmigrating tides from TIMED Doppler Interferometer wind data: Monthly climatologies and seasonal variations, *J. Geophys. Res.*, *111*, A10S03, doi:10.1029/2005JA011491.
- Onwumechili, C. A. (1967), *Geomagnetic Variations in the Equatorial Zone of Peru Physics of Geomagnetic Phenomena-I*, pp. 425–507, Academic Press, New York.
- Onwumechili, C. A., and C. E. Agu (1980), General features of the magnetic field of the equatorial electrojet measured by the POGO satellites, *Planet. Space Sci.*, *28*, 1125–1130, doi:10.1016/0032-0633(80)90071-9.
- Venkatesh, K., P. R. Fagundes, D. S. V. D. Prasad, C. M. Denardini, A. J. de Abreu, R. de Jesus, and M. Gende (2015), Day-to-day variability of equatorial electrojet and its role on the day-to-day characteristics of the equatorial ionization anomaly over the Indian and Brazilian sectors, *J. Geophys. Res. Space Physics*, *120*, 9117–9131, doi:10.1002/2015JA021307.
- Wu, Q., D. A. Ortland, B. Foster, and R. G. Roble (2012), Simulation of nonmigrating tide influences on the thermosphere and ionosphere with a TIMED data driven TIEGCM, *J. Atmos. Sol. Terr. Phys.*, *90–91*, 61–67, doi:10.1016/j.jastp.2012.02.009.
- Xiong, C., and H. Lühr (2013), Nonmigrating tidal signatures in the magnitude and the inter-hemispheric asymmetry of the equatorial ionization anomaly, *Ann. Geophys.*, *31*, 1115–1130, doi:10.5194/angeo-31-1115-2013.
- Xiong, C., H. Lühr, and B. G. Fejer (2016), The response of equatorial electrojet, vertical plasma drift and thermospheric zonal wind to enhanced solar wind input, *J. Geophys. Res. Space Physics*, *121*, 5653–5663, doi:10.1002/2015JA022133.
- Yamazaki, Y., and M. J. Kosch (2015), The equatorial electrojet during geomagnetic storms and substorms, *J. Geophys. Res. Space Physics*, *120*, 2276–2287, doi:10.1002/2014JA020773.
- Yamazaki, Y., A. D. Richmond, A. Maute, H.-L. Liu, N. Pedatella, and F. Sassi (2014), On the day-to-day variation of the equatorial electrojet during quiet periods, *J. Geophys. Res. Space Physics*, *119*, 6966–6980, doi:10.1002/2014JA020243.